A Study of Needle Image Artifact Localization in Confirmation Imaging of MRI-guided Robotic Prostate Biopsy

Sang-Eun Song,
Laboratory for Computational Sensing and Robotics (LCSR) and Department of Mechanical Engineering (ME), Johns Hopkins University (JHU), Baltimore, Maryland, USA

Nathan B. Cho,
Laboratory for Computational Sensing and Robotics (LCSR) and Department of Mechanical Engineering (ME), Johns Hopkins University (JHU), Baltimore, Maryland, USA

Iulian I. Iordachita,
Laboratory for Computational Sensing and Robotics (LCSR) and Department of Mechanical Engineering (ME), Johns Hopkins University (JHU), Baltimore, Maryland, USA

Peter Guion,
Radiation Oncology Branch, National Cancer Institute, National Institutes of Health, Bethesda, Maryland, USA

Gabor Fichtinger, and
School of Computing, Queen's University, Kingston, Ontario, Canada

Louis L. Whitcomb
Laboratory for Computational Sensing and Robotics (LCSR) and Department of Mechanical Engineering (ME), Johns Hopkins University (JHU), Baltimore, Maryland, USA

Abstract

Recently several systems for magnetic resonance image (MRI) guided needle placement in the prostate have been reported. In comparison to conventional ultrasound-guided needle placement in the prostate, these MRI-guided systems promise improved targeting accuracy for prostate intervention procedures including biopsy, fiducial marker insertion, injection and focal therapy. In MRI-guided needle interventions, after a needle is inserted, the needle position is often confirmed with a volumetric MRI scan. Commonly used titanium needles are not directly visible in an MR image, but they generate a susceptibility artifact in the immediate neighborhood of the needle. This paper reports the results of a quantitative study of the relation between the true position of titanium biopsy needle and the corresponding needle artifact position in MR images. The titanium needle artifact was found to be displaced 0.38 mm and 0.32 mm shift in scanner's frequency and phase encoding direction, respectively. The artifact at the tip of the titanium needle was observed to bend toward the scanner's B_0 magnetic field direction.

I. Introduction

To confirm the accuracy of MRI-guided needle targeting, a confirmation image is acquired while the needle is inserted so that the clinician can evaluate the needle placement accuracy. Titanium biopsy needles are not directly visible in an MRI image, but they generate a susceptibility artifact in the MR image in the neighborhood of the titanium needle. This

Corresponding author: S. Song, sam0song@gmail.com.

artifact is commonly termed a 'needle void' or 'needle artifact'. The needle artifact is typically displaced from the true needle position, and differs in size and shape from the needle itself. This paper reports the results of a quantitative study of the relation between the true position of titanium biopsy needle and the corresponding needle artifact position in MR images.

A. Prostate Cancer Diagnosis

Prostate cancer is the most common cancer in men in the United States. In 2010, an estimated 217,730 men will be diagnosed with prostate cancer and 32,050 will die of this disease [1]. Each year approximately 1.5 million prostate biopsy procedures are performed.

The two commonly used methods for screening men for prostate cancer are the prostate-specific antigen (PSA) blood test and the digital rectal exam (DRE). The American Cancer Society recommends screening men, beginning at age 50, yearly with PSA test and DRE. The definitive diagnosis for prostate cancer is core needle biopsy pursuant to either an elevated PSA level or a positive DRE. The 'Gold Standard' of guiding biopsy, as well as of most local therapies, is transrectal ultrasound (TRUS) [2]. The physician manually places a TRUS probe in the rectum of the patient and, under ultrasound guidance, inserts a biopsy needle through the wall of the rectum into the prostate gland. The needle removes a half-cylinder of tissue, which is examined pathologically to determine if cancer is present. Several biopsy samples are taken from different areas of the prostate. Usually six (hence 'sextant biopsy') to eighteen cores are removed from upper, mid, and lower areas of the left and right sides to obtain a representative sample of the gland and determine the degree and extent of cancer.

B. TRUS-guided Prostate Biopsy

TRUS-guided prostate biopsy is widely employed due to its real-time nature, relative low cost, and ease of use. Using standard techniques, biopsy of men with PSA values in the range of 4–10 ng/ml generally result in a detection rate of 20%–30% [3]. Numerous studies have shown that TRUS-guided prostate biopsy fails to detect cancer in at least 20% of patients with cancer [4]. Other studies report that TRUS biopsies are limited by low sensitivity of 60% with only 25% positive predictive value [5]. TRUS imaging is generally unable to differentiate between healthy tissue and lesions in the prostate. In consequence, contemporary TRUS-guided biopsy cannot identify or target lesions, but rather samples six or more representative locations in the gland. Studies of the efficacy of 6 versus 12 biopsy samples show no significant difference in cancer detection [6]. This suggests that increase in the number of samples does not solve the problem of prostate cancer detection, and that improved biopsy targeting may be advantageous.

II. MRI-guided Prostate Interventions

MRI possesses many of the capabilities that TRUS is lacking. MRI is an attractive choice for image guidance, primarily due to its high sensitivity for detecting prostate tumors [7], high spatial resolution, excellent soft tissue contrast, and multi-planar volumetric imaging capabilities.

A. MRI-Guided Prostate Needle Intervention Systems

Several different systems for MRI-guided needle access of the prostate have been reported. They include the following:

1. Transrectal Approach: In [8] the authors reported the development and clinical evaluation of a MRI-guided system for transrectal prostate biopsies, therapy injection, and marker placements. The system, called the APT, contains a single-

loop MRI endorectal imaging coil and employs active or passive tracking for device localization. In vivo and in vitro accuracy results were reported. This clinical prototype has been successfully used in over 50 patient procedures to date. Beyersdorff [9] and Engelhard [10] report MRI-guided transrectal needle biopsies in clinical studies with a system (Invivo Germany GmbH, Schwerin, Germany) employing manual alignment of a needle sleeve. In [11] Schouten reports a MRI-compatible pneumatically actuated transrectal robot. Elhawary reported a prototype robotic system using linear piezoceramic motors for transrectal prostate biopsy [12].

2. Transperineal Approach: MRI-guided transperineal prostate intervention has been demonstrated in clinical studies inside in open MRI scanners [13] and in conventional closed MRI scanners [14]. The surgical assistant robot reported by Chinzei [15] was adapted to assist transperineal intra-prostatic needle placement [16]. Tadakuma reported the use of dielectric elastomer actuators in a pre-clinical prototype robot for transperineal needle placement in the prostate [17]. Stoianovici reported pre-clinical phantom experiments with a pneumatic system for transperineal brachytherapy [18]. In [19, 20], the authors report phantom experiments with a device with a pneumatically actuated needle guide and manual needle insertion for transperineal needle placement in the prostate. Goldenberg reported phantom targeting and MRI compatibility tests for a robotic system employing ultrasonic actuators for closed MRI scanners [21]. In [22], van den Bosch reported a hydraulically and pneumatically actuated tapping robot.

3. Transgluteal Approach: Zangos reported preliminary clinical results with 25 patients using the transgluteal approach with an open configuration 0.2T MRI scanner [23], with targeting based on prior diagnostic images acquired with higher field strength MRI. In [24], Zangos reported usage of the Innomotion pneumatic robot in a cadaver study at 1.5T for transgluteal prostate needle placements.

B. Previously Reported MRI Needle Artifact Studies

Blumenfeld [25] reported that needle placement error is mainly from the needle deflection especially with asymmetrically beveled tip needle. Lullcin [26] described a technique for MRI-guided needle placement by selectively rotating the scan plane. Lewin [27] reported a needle artifact study to evaluate MR imaging accuracy at 0.2T and 1.5T with multiple sequences and needle rotations. When the needle is perpendicular to the frequency encoding direction and the static magnetic field (B_0), the artifacts are much apparent. DiMaio [28] conducted a needle artifact study in 3T MRI using a rotating needle holder with ex-vivo tissue sample, concluding that artifacts are shifted along the frequency encoding direction.

Wachowicz [29] modeled seed artifacts in various directions with respect to B_0 to create distortion maps, and compared these simulated images to actual imagery. The results indicated good agreement suggesting that artifact patterns depended on the encoding direction and orientations of the B_0 field and seed. Lagerburg [30] studied artifacts of iodine seeds placed at the needle tip in MRI guided prostate brachytherapy, reporting that determination of the exact seed position was difficult because of the large artifact at the tip of the needle. Thomas [31] also investigated the effects of artifact size on the ability to localize multiple seeds in close proximity.

III. Methods

A series of preliminary tests revealed that variation in titanium needle size (14G, 16G and 18G) had little effect on needle void size and shape, hence a 14G biopsy needle was employed in the experiments reported herein. Commercially available prostate phantoms

have limited target volume, and their multiple layers may cause needle bending during insertion. Hence, a larger and uniformly soft customized gel phantom was tested and selected for the experiment.

A. Experiment Setup

Fig. 1 shows a needle artifact experiment setup using the APT robot, [8], in 3T Philips Achieva MRI scanner (Philips Medical Systems, Best, NL). A custom made gel phantom (plant starch mixed with water and heated) was used as a soft tissue phantom. The phantom was placed on the scanner table between two liquid imaging phantoms. In order to identify the true needle position, a 14 gauge sized glass rod with conical tip was used. For the needle artifact, a 150 mm 14G MRI-compatible automatic titanium biopsy gun (product number: 11705, Invivo, Orlando, Florida, USA), which is routinely used for patient procedures, was employed. The titanium needle has a bevel tip but the beveled direction was not considered in the experiment since the bevel angle is not actively controlled in the robotic procedures. An endorectal imaging coil embedded in the APT robot was used to obtain T2-weight axial Turbo Spin Echo (TSE) images (Table 1) of the glass rod and titanium needle.

B. Needle Placement

After the robot and phantom were securely positioned, a series of registration scans were obtained to determine the location of four fiducial markers (Beekley Corp., Bristol, CT), which are embedded in the APT robot at predefined positions. 3D Slicer with ProstatNav module (www.slicer.com) was used. The ProstatNav software module is designed for APT robot registration, targeting and evaluation. However, in this experiment, only registration was performed as no target was required to guide pre-planned needle insertion angles. Fig. 2 shows a screenshot of 3D Slicer ProstateNav module.

To observe the needle artifact in various needle orientations, fifteen distinct needle orientations, comprised of five roll angles and three pitch angles, were selected. In the preliminary tests, no noticeable artifact variation was observed with insertion depth variation, so an insertion depth of 140 mm was employed uniformly. The fifteen orientations were manually set in sequence. At each insertion orientation, a glass rod was first inserted and a confirmation image taken, then the 14G titanium biopsy needle was inserted and a confirmation image taken. In total, 30 sets (five roll angle and three pitch angle for each of the glass rod and titanium needle) of volumetric confirmation images were obtained. Fig. 3 illustrates a CAD model of needle insertion angles in scanner's RAS coordinate.

C. Finding Needle Artifact Axis

The center of the needle artifact was selected manually in each of the image slices of all 30 volumetric scans. Fig. 4 shows a series of cropped images that represent typical artifact patterns of glass rod and titanium needle.

The manually selected needle-artifact center positions were then used to compute the least-square fit to a line in three-dimensional space. The titanium needle tip creates distinctive artifact that deviates from needle body artifact in both size and direction. Hence, the titanium needle tip artifact, which appears beyond glass rod tip, was excluded from the least square solution.

IV. Results

Thirty volumetric MR axial volumetric scans of needles were analyzed with the needles positioned in fifteen distinct needle positions to identify the center of the needle image artifact in each of the axial image slices. For each of fifteen needle guide positions two scans

were analyzed: one volumetric confirmation scan of 14G titanium biopsy needle and one confirmation scan of the 14G glass rod, for a total of 30 volumetric confirmation scans.

A. Needle Artifact Geometry

Fig. 5 shows sagittal and coronal views of the needle void locations observed on each axial slice for the titanium needle and glass rod and their corresponding least-square best-fit lines. For the axial image slices in which the needles were present, the centers of the voids for both the glass rod and titanium needle were found to be linear.

Table 2 reports the RMS residuals (mm) for the least square line fits for each of the 15 insertion positions for the glass rod (Table 2, top) and titanium needle (Table 2, bottom). This table shows that the RMS residuals for both the glass rod and titanium needle to be much smaller than the pixel width of 0.859 mm. The typical value is under 0.1 mm, an order of magnitude less than the pixel width. The maximum observed RMS residual was 0.169 mm. These data show that for both the glass and titanium needle are co-linear.

The needle void created by titanium needles in MR images extend beyond the physical tip of the needle. In these images, the titanium needle void was present in three axial slices (i.e. a total of 9 mm) beyond the physical tip of the needle itself. Moreover, this extension of the titanium needle artifact exhibited a pronounced curvature in the direction of the B_0 magnetic field. This pronounced effect is shown in Fig. 7.

B. Titanium Needle Artifact Localization

The axial-plane needle artifact position errors for the fifteen tested needle orientations are given in Fig. 6. The plots show the axial plane difference between the center of the titanium needle void and the center of the glass rod void for all axial image slices physically intersecting the needles. The actual needle locations are physically identical in each case, but the titanium needle image void is displaced with respect to the actual needle position that is given by the glass rod.

These data indicate the titanium needle void is consistently displaced in the Y (anterior) frequency encoding direction. At needle tilt angles of 18° the median Y displacement was small but varied from −0.7 mm to +0.1 mm, but with a large standard deviation of 0.90 mm to 0.99 mm. At needle tilt angles of 28° the median Y displacement varied from +0.90 mm to +1.44 mm, with a moderate standard deviation of 0.23 mm to 0.56 mm. At needle tilt angles of 38° the median Y displacement varied from 0.90 mm to +1.44 mm, with a comparatively small standard deviation of 0.22 mm to 0.57 mm.

These data show the titanium needle void is inconsistently displaced in X (right) phase encoding direction. The needle displacements in the phase encoding direction all have means of magnitude 0.5 mm or less, and very small standard deviations of 0.4 mm or less.

Table 3 shows the axial-plane needle artifact position error mean and standard deviation averaged over the fifteen tested needle orientations. The average displacement in the Y (anterior) frequency encoding direction is 0.38 mm with a comparatively large standard deviation of 0.56 mm. The average displacement in the X (right) phase encoding direction is 0.32 mm with a comparatively small standard deviation of 0.13 mm.

V. Conclusion

We conclude the following:

1. The titanium needle-void artifacts in T2 confirmation imagery form a straight line parallel to the actual needle position in slices in which the needle is physically present.

2. The needle tip artifact can extend 9 mm beyond the actual needle tip location, and it exhibits strong curvature in the direction of the B_0 magnetic field.

3. The magnitude of the titanium needle void displacement increases monotonically with the needle's angle with respect to the scanner's B_0 magnetic field direction.

4. The needle void displacement is systematic in the Y (anterior) frequency encoding direction, and with large variance. This corroborates previous reports [27, 28].

5. The needle void displacement is smaller in the X (right) phase encoding direction, with small variance.

6. All of the observed titanium needle void artifact displacements are 2 mm or less from the actual needle location, smaller than the radius of the clinically significant tumor size of approximately 4.9 mm [32].

Acknowledgments

References

1. American Cancer Society. Cancer Facts and Figures 2010. American Cancer Society; Atlanta: 2010.

2. Presti JC. Prostate cancer: assessment of risk using digital rectal examination, tumor grade, prostate-specific antigen, and systematic biopsy. Radiologic Clinics of North America. Jan; 2000 38(1):49–58. [PubMed: 10664666]

3. Roehl KA, Antenor JAV, Catalona WJ. Serial biopsy results in prostate cancer screening study. Journal of Urology. Jun; 2002 167(6):2435–2439. [PubMed: 11992052]

4. Wefer AE, Hricak H, Vigneron DB, Coakley FV, Lu Y, Wefer J, Mueller-Lisse U, Carroll PR, Kurhanewicz J. Sextant localization of prostate cancer: comparison of sextant biopsy, magnetic resonance imaging and magnetic resonance spectroscopic imaging with step section histology. Journal of Urology. Aug; 2000 164(2):400–404. [PubMed: 10893595]

5. Keetch DW, McMurtry JM, Smith DS, Andriole GL, Catalona WJ. Prostate specific antigen density versus prostate specific antigen slope as predictors of prostate cancer in men with initially negative prostatic biopsies. Journal of Urology. Aug; 1996 156(2 Pt 1):428–431. [PubMed: 8683695]

6. O'Connell MJ, Smith CS, Fitzpatrick PE, Keane CO, Fitzpatrick JM, Behan M, Fenlon HF, Murray JG. Transrectal ultrasound-guided biopsy of the prostate gland: value of 12 versus 6 cores. Abdominal Imaging. 2004; 29(1):132–136. [PubMed: 15160768]

7. Pondman KM, Ftterer JJ, ten Haken B, Kool LJS, Witjes JA, Hambrock T, Macura KJ, Barentsz JO. Mr-guided biopsy of the prostate: an overview of techniques and a systematic review. Eur Urol. Sep; 2008 54(3):517–527. [PubMed: 18571309]

8. Krieger A, Susil RC, Menard C, Coleman JA, Fichtinger G, Atalar E, Whitcomb LL. Design of a novel MRI compatible manipulator for image guided prostate interventions. IEEE Transactions on Biomedical Engineering. Feb; 2005 52(2):306–313. [PubMed: 15709668]

9. Beyersdorff D, Winkel A, Hamm B, Lenk S, Loening SA, Taupitz M. MR imaging-guided prostate biopsy with a closed MR unit at 1.5T: Initial results. Radiology. February; 2005 234(2):576–581. [PubMed: 15616117]

10. Engelhard K, Hollenbach HP, Kiefer B, Winkel A, Goeb K, Engehausen D. Prostate biopsy in the supine position in a standard 1.5-T scanner under real time MR-imaging control using a MR-

compatible endorectal biopsy device. European Radiology. Jun; 2006 16(6):1237–1243. [PubMed: 16447048]

11. Schouten MG, Ansems J, Renema WK, Bosboom D, Scheenen TWJ, Futterer JJ. The accuracy and safety aspects of a novel robotic needle guide manipulator to perform transrectal prostate biopsies. Med Phys. 2010; 37(9):4744–4750. [PubMed: 20964192]

12. Elhawary H, Zivanovic A, Rea M, Davies B, Besant C, McRobbie D, de Souza N, Young I, Lamprth M. The feasibility of MRimage guided prostate biopsy using piezoceramic motors inside or near to the magnet isocentre. International Conference on Medical Image Computing and Computer-Assisted Intervention. 2006; 9(Pt 1):519–526.

13. D'Amico AV, Tempany CM, Cormack R, Hata N, Jinzaki M, Tuncali K, Weinstein M, Richie JP. Transperineal magnetic resonance image guided prostate biopsy. Journal of Urology. Aug; 2000 164(2):385–387. [PubMed: 10893591]

14. Susil R, Camphausen K, Choyke P, McVeigh E, GGGS, Ning H, Miller R, Atalar E, Coleman C, Menard C. System for prostate brachytherapy and biopsy in a standard 1.5T MRI scanner. Magnetic Resonance in Medicine. September; 2004 52(3):683–7. [PubMed: 15334592]

15. Chinzei K, Hata N, Jolesz FA, Kikinis R. MRI compatible surgical assist robot: System integration and preliminary feasibility study. Medical Image Computing and Computer-Assisted Intervention (MICCAI). 1935 October.:921–930. 2000.

16. DiMaio SP, Pieper S, Chinzei K, Hata N, Haker SJ, Kacher DF, Fichtinger G, Tempany CM, Kikinis R. Robot-assisted needle placement in open MRI: system architecture, integration and validation. Comput Aided Surgery. Jan; 2007 12(1):15–24.

17. Tadakuma K, DeVita L, SY, Dubowsky S. The experimental study of a precision parallel manipulator with binary actuation: With application to MRI cancer treatment. Proc IEEE International Conference on Robotics and Automation ICRA '08. May 21–23.2008 :2503–2508.

18. Stoianovici D, Song D, Petrisor D, Ursu D, Mazilu D, Muntener M, Mutener M, Schar M, Patriciu A. MRI stealth robot for prostate interventions. Minimally Invasive Therapy and Allied Technologies. 2007; 16(4):241–248. [PubMed: 17763098]

19. Fischer GS, Iordachita I, Csoma C, Tokuda J, DiMaio SP, Tempany CM, Hata N, Fichtinger G. MRI-compatible pneumatic robot for transperineal prostate needle placement. IEEE/ASME Transactions on Mechatronics. June; 2008 13(3):295–305. [PubMed: 21057608]

20. Song, S-E.; Cho, NB.; Fischer, G.; Hata, N.; Tempany, C.; Fichtinger, G.; Iordachita, I. Development of a pneumatic robot for mri-guided transperineal prostate biopsy and brachytherapy: New approaches. Proc. IEEE Int Robotics and Automation (ICRA) Conf; 2010. p. 2580-2585.

21. Goldenberg AA, Trachtenberg J, Kucharczyk W, Yi Y, Haider M, Ma L, Weersink R, Raoufi C. Robotic system for closed bore MRI-guided prostatic interventions. IEEE/ASME Transactions on Mechatronics. June; 2008 13(3):374–379.

22. van den Bosch MR, Moman MR, van Vulpen M, Battermann JJ, Duiveman E, van Schelven LJ, de Leeuw H, Lagendijk JJW, Moerland MA. Mri-guided robotic system for transperineal prostate interventions: proof of principle. Phys Med Biol. Mar; 2010 55(5):N133–N140. [PubMed: 20145293]

23. Zangos S, Eichler K, Engelmann K, Ahmed M, Dettmer S, Herzog C, Pegios W, Wetter A, Lehnert T, Mack MG, Vogl TJ. MRguided transgluteal biopsies with an open low-field system in patients with clinically suspected prostate cancer: technique and preliminary results. European Radiology. Jan; 2005 15(1):174–182. [PubMed: 15351902]

24. Zangos S, Herzog C, Eichler K, Hammerstingl R, Lukoschek A, Guthmann S, Gutmann B, Schoepf UJ, Costello P, Vogl TJ. MR-compatible assistance system for punction in a high-field system: device and feasibility of transgluteal biopsies of the prostate gland. European Radiology. Apr; 2007 17(4):1118–1124. [PubMed: 17031454]

25. Blumenfeld P, Hata N, DiMaio S, Zou K, Haker S, Fichtinger G, Tempany CMC. Transperineal prostate biopsy under magnetic resonance image guidance: a needle placement accuracy study. Journal of Magnetic Resonance Imaging. Sep; 2007 26(3):688–694. [PubMed: 17729363]

26. Lullcin R, Teresi L, Chiu L, Hanafee W. A technique for MR-guided needle placement. American Journal of Roentgenology. 1988; 151:193–196. [PubMed: 3259804]

27. Lewin JS, Duerk JL, Jain VR, Petersilge CA, Chao CP, Haaga JR. Needle Localization in MR-Guided Biopsy and Aspiration. American Journal of Radiology. 1996; 166:1337–1345.

28. DiMaio SP, Kacher DF, Ellis RE, Fichtinger G, Hata N, Zientara GP, Panych LP, Kikinis R, Jolesz FA. Needle artifact localization in 3t MR images. Stud Health Technol Inform. 2006; 119:120–125. [PubMed: 16404029]

29. Wachowicz K, Thomas SD, Fallone BG. Characterization of the susceptibility artifact around a prostate brachytherapy seed in MRI. Med Phys. 2006 Dec; 33(12):4459–67. [PubMed: 17278797]

30. Lagerburg V, Moerland MA, Seppenwoolde JH, Lagendijk JJ. Simulation of the artefact of an iodine seed placed at the needle tip in MRI-guided prostate brachytherapy. Phys Med Biol. 2008 Mar 7; 53(5):N59–67. [PubMed: 18296753]

31. Thomas SD, Wachowicz K, Fallone BG. MRI of prostate brachytherapy seeds at high field: a study in phantom. Med Phys. 2009 Nov; 36(11):5228–34. [PubMed: 19994533]

32. Nakashima J, Tanimoto A, Imai Y, Mukai M, Horiguchi Y, Nakagawa K, Oya M, Ohigashi T, Marumo K, Murai M. Endorectal MRI for prediction of tumor site, tumor size, and local extension of prostate cancer. Urology. Jul; 2004 64(1):101–105. [PubMed: 15245944]
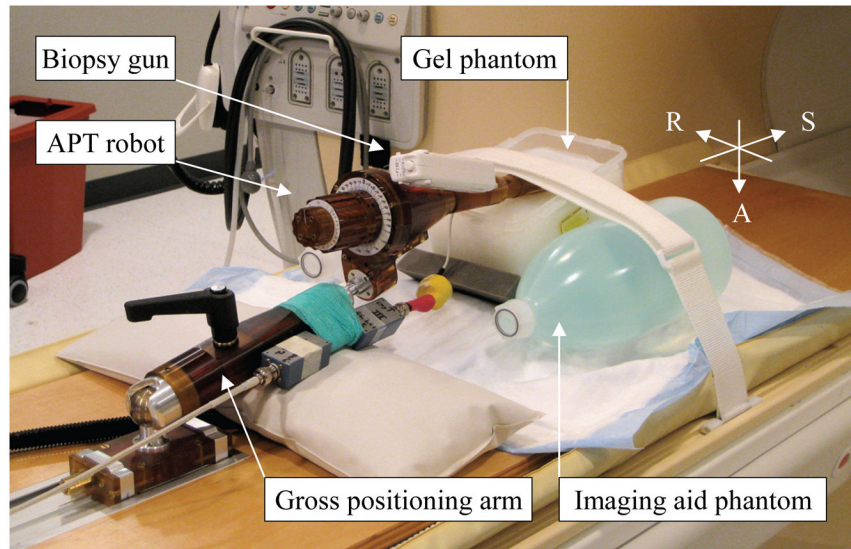
Fig. 1.
Photograph of needle artifact study experimental setup, showing APT transrectal prostate interventional robot with a 14 gauge biopsy gun inserted into custom made gel phantom in 3T Philips Achieva MRI scanner.
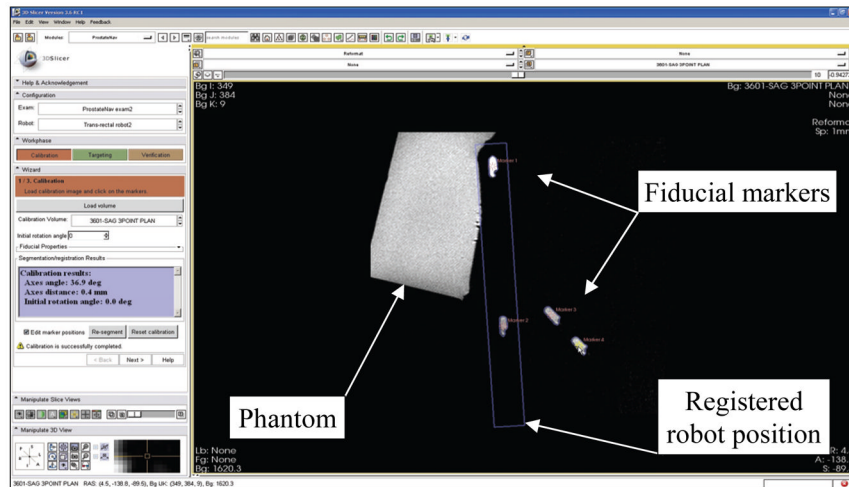
Fig. 2.
A screenshot of APT robot registration in 3D Slicer ProstateNav module. In the marker plane sagittal view, four embedded fiducial markers are identified to locate the robot position in scanner space.
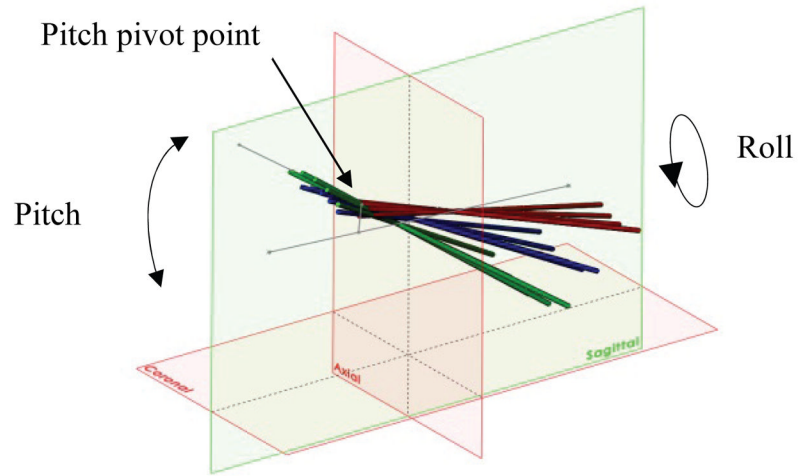
Fig. 3.
CAD model of various needle insertion angles: pitch angle of 18, 28, 38 degrees and roll angle of −30, −15, 0, 15, 30 degrees. Grey colored reference lines represent initial needle insertion axis, roll axis and the line between roll axis and the pivot point of pitch angle.
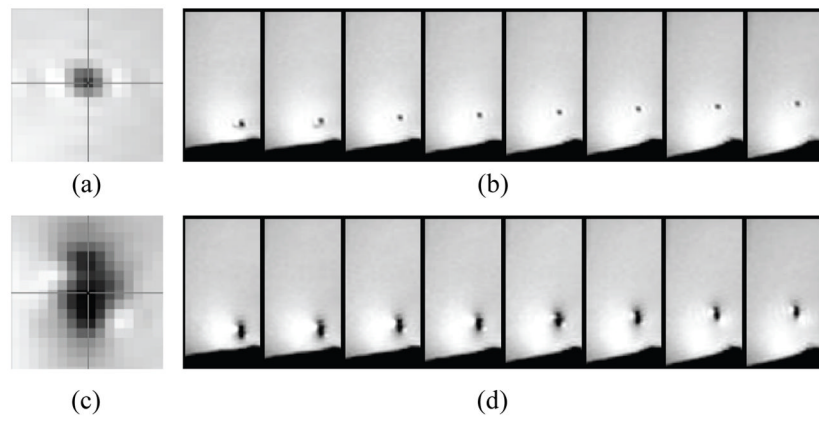
Fig. 4.
Representative images of glass rod and titanium needle artifact: (a) zoomed view of typical glass rod artifact, (b) glass rod artifact images from inferior to superior direction (left to right), (c) and (d) are of titanium needle.
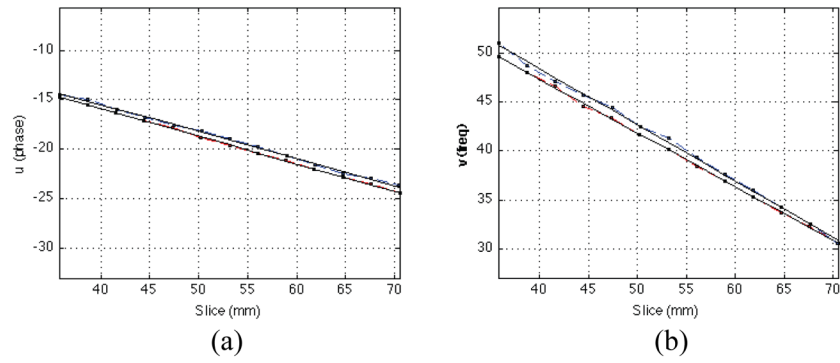
Fig. 5.
MRI needle void locations for titanium needle (blue) and glass rod (red) and corresponding least-square best fit lines (solid black lines). Left plot shows coronal view with phase-encoding direction along the Y-axis, and the B_0-field along the X-axis. Right plot shows sagittal view with frequency encoding direction along the Y-axis and the B_0-field along the X-axis.
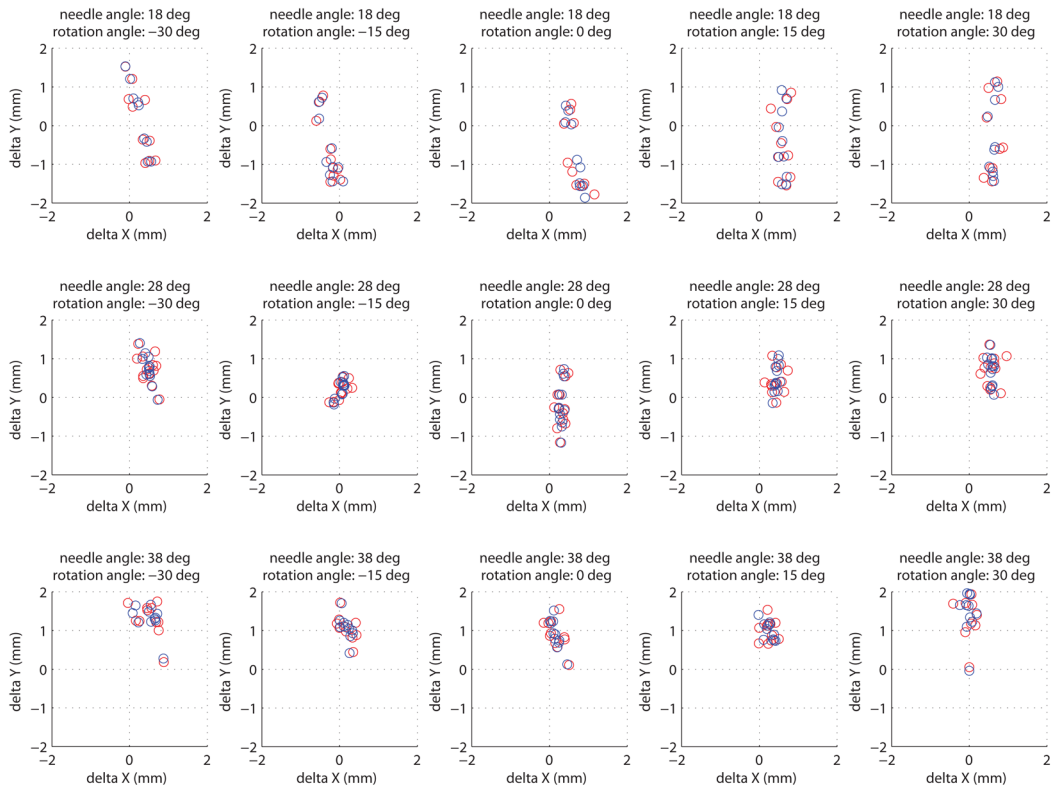
Fig. 6.
Axial-plane needle artifact position error for the fifteen tested needle orientations. The plots show the axial plane difference between the center of the titanium needle void and the center of the glass rod void for all axial image slices physically intersecting the needles. The needle locations are physically identical, but the titanium needle image void is displaced with respect to the actual needle position that is given by the glass rod. The rows represent needle tilt angles of (from top to bottom) +18°, +28°, and +38°. The columns represent needle rotation angles of −30°, −15°, 0°, +15°, +30°. 'delta X' and 'delta Y' represent R (right) and A (anterior) coordinate directions in scanner coordinate, respectively. Blue circle data represents the error value from manually located artifact center position, and red circle data represents that from fitted line as seen in Fig. 5.
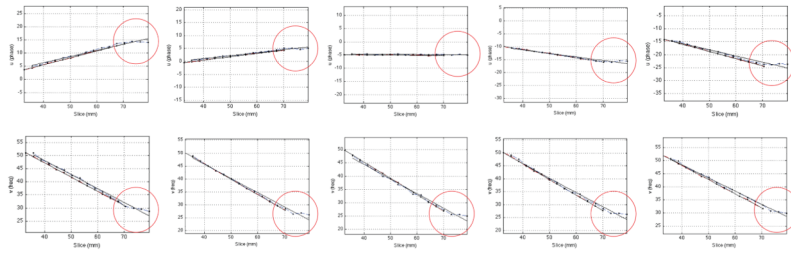
Fig. 7.
Representative plots of glass rod and titanium needle artifact center positions and fitted line at various insertion angles including entire recognizable titanium needle artifact, showing "bending" of the titanium needle tip artifact towards B_0 direction (red circle). First row: coronal plane plots of −30, −15, 0, 15, 30 degree roll angles (from left) with 28 degree pitch angle, second row: corresponding sagittal plane plots.

Table 1

MRI scan parameters for needle artifact study

Slice thickness (mm)	3
Number of pixel	256×256
Pixel size (mm)	0.859375
Field of view (mm)	220×256
Number of slices	28
TE (echo time) (ms)	70
TR (repetition time) (ms)	11416
Flip angle (°)	90
NEX (number of excitations)	1
Pixel bandwidth (Hz/pixel)	1554

Table 2

RMS residuals (mm) for the least square line fits for each of the 15 insertion positions for the glass rod (top) and titanium needle (bottom).

Glass rod RMS line fit residuals (mm)					
	Rotation angle (deg)				
Needle angle (deg)	**−30**	**−15**	**0**	**15**	**30**
18	0.036	0.045	0.092	0.087	0.096
28	0.055	0.072	0.075	0.062	0.066
38	0.123	0.072	0.087	0.050	0.089

Titanium needle RMS line fit residuals (mm)					
	Rotation angle (deg)				
Needle angle (deg)	−30	−15	0	15	30
18	0.108	0.063	0.092	0.146	0.122
28	0.120	0.092	0.089	0.102	0.154
38	0.169	0.093	0.089	0.138	0.143

Table 3

Axial-plane needle artifact position error mean and standard deviation averaged over the fifteen tested needle orientations. 'delta X' and 'delta Y' represent R (right) and A (anterior) coordinate directions in scanner coordinate, respectively.

	delta X (mm)	delta X std (mm)	delta Y (mm)	delta Y std (mm)
Titanium – Glass (manual)	0.32	0.19	0.38	0.57
Titanium – Glass (fitted line)	0.32	0.13	0.38	0.56